Turbulent mixing with physical mass diffusion

Xinfeng Liu,[1] Erwin George,[1] Wurigen Bo,[1] and J. Glimm[1,2]
[1]*Department of Applied Mathematics and Statistics, Stony Brook University, Stony Brook, New York 11794-3600, USA*
[2]*Computational Science Center, Brookhaven National Laboratory, Upton, New York 11793-6000, USA*
(Received 4 January 2006; published 1 May 2006)

Simulated mixing rates of the Rayleigh-Taylor instability for miscible fluids with physical mass diffusion are shown to agree with experiment; for immiscible fluids with physical values of surface tension the numerical data lie in the center of the range of experimental values. The simulations are based on an improved front tracking algorithm to control numerical surface tension and on improved physical modeling to allow physical values of mass diffusion or surface tension. Compressibility, after correction for variable density effects, has also been shown to have a strong influence on mixing rates. In summary, we find significant dependence of the mixing rates on scale breaking phenomena. We introduce tools to analyze the bubble merger process and confirm that bubble interactions, as in a bubble merger model, drive the mixing growth rate.

DOI: 10.1103/PhysRevE.73.056301 PACS number(s): 47.27.−i, 47.40.−x, 47.52.+j

I. INTRODUCTION

The dynamical equations governing fluid flow are based on the principles of conservation of mass, momentum, and energy. The front tracking code FRONTIER [1–5] has been used to study the Euler equations for many years. It has been shown to be successful, especially for flows dominated by complex fluid interfaces and mixing processes.

To model the mixing of compressible miscible fluids with mass diffusion, the conservation equations take the form

$$\frac{\partial \rho}{\partial t} + \nabla \cdot (\rho u) = \nu \Delta \rho,$$

$$\frac{\partial \rho u}{\partial t} + \nabla \cdot (\rho u u) = \nabla P + \rho g + \nu \nabla \cdot (u \nabla \rho),$$

$$\frac{\partial (\rho E)}{\partial t} + \nabla \cdot [(\rho E + P)u] = \nu \nabla \cdot (E \nabla \rho) + \rho u g. \qquad (1)$$

Here ν is the coefficient of mass diffusion, ρ is density, u is velocity, P is pressure, g is gravity, and E is total specific energy. To complete the system, an equation of state (EOS) relating the state variables is necessary. We use a gamma law gas with $\gamma = 1.67$.

The Rayleigh-Taylor (RT) instability occurs when a fluid of low density ρ_l accelerates a fluid of heavy density ρ_h. It occurs in astrophysics (supernova), geophysics, and technology (inertially confined fusion) among other subjects. The RT mixing rate is the dimensionless coefficient α in the equation

$$h = \alpha A g t^2 \qquad (2)$$

for the height h of the bubbles, i.e., the interpenetration distance h of the light fluid into the heavy fluid. Here $A = (\rho_h - \rho_l)/(\rho_h + \rho_l)$ is the Atwood number and t is the time. Acceptable experimental values for α are $\alpha = 0.063 \pm 0.013$ [6–10]. See Ref. [11] for background information.

The main purpose of this paper is to use an improved front tracking algorithm allowing limited physical (but not numerical) mass diffusion across a tracked interface and to validate this algorithm through the simulation of three-dimensional (3D) Rayleigh-Taylor mixing of miscible fluids, obtaining agreement with experimental data. The rest of the paper is organized as follows. Section II discusses length scales and dispersion relations to set initial conditions equivalent under change of scale transformations to experiments. Section III describes the physical mass diffusion effect on the turbulent mixing rates. We find a simulation value of $\alpha = 0.069$ in comparison to the experimental value [9] $\alpha = 0.07$, and in contrast to the ideal (zero diffusion) simulation value $\alpha = 0.09$ [12]. We also summarize previous results showing simulation agreement with experiment for immiscible fluids with physical values of surface tension [12]. We analyze a conventional untracked total variation diminishing (TVD) simulation [13] of the same problem for ideal fluids, determine its effective value of numerical mass diffusion, and discuss a grid related interface smoothing effect which could be interpreted as numerical surface tension. We explore the role of compressibility on mixing rates. We find an increase in mixing rates with increasing compressibility after removing variable Atwood number effects.

In Sec. IV, we study the bubble merger process based on our current simulations. Our results confirm a number of the hypotheses and conclusions of the bubble merger models, and serve to justify their application to RT mixing.

Finally, the results are summarized in Sec. V. The substantial agreement with experiments for the simulation of real fluid mixing rates with physical mass diffusion or surface tension and the strong dependence of variable density corrected RT mixing rates on compressibility indicate that scale breaking phenomena are important in simulating the Rayleigh-Taylor instability.

II. DISPERSION RELATIONS

In order to compare simulations to experiment, we do not attempt to duplicate exactly all experimental conditions. Rather we apply a change of scale, and attempt to duplicate dimensionless parameters which characterize the experi-

 ©2006 The American Physical Society

TABLE I. Summary of length scales and scale breaking parameters for various RT turbulent mixing experiments.

Experiment	Scale breaking physics	λ observed (cm)	λ theory (cm)	Parameter observed (dimensionless)	Parameter theory (dimensionless)
Immiscible [8,6]	surface tension	0.41–0.54	0.37–0.45	4.6–8.8 $\times 10^{-3}$	8.5 $\times 10^{-3}$
Miscible [6]	viscosity initial mixing layer	0.38	0.21–0.25	3.9–2.25 $\times 10^{-4}$	0.73–1.05 $\times 10^{-3}$
Miscible [7]	viscosity diffusion	5	0.44–0.86	7.33–8.11 $\times 10^{-4}$	2.06–2.39 $\times 10^{-2}$
Miscible [9]	mass diffusion	0.5	6.61–8.37	0.19–0.31	3.97–4.54 $\times 10^{-3}$

ments. The Rayleigh-Taylor experiments are for the most part strongly incompressible, and simulation in this regime is not practical with a compressible code, so we are content with reduction of the dimensionless compressibility to sufficiently small values so that the incompressible limit has been attained numerically. Similarly, we do not attempt to duplicate the very large number of different Atwood numbers present in the experiments, as the scaling properties of this variable are well understood. Physical values of the scale breaking parameters are available from published sources, especially if we ignore refinements such as temperature dependence for quantities slowly varying over a presumed range of experimental temperatures. See Ref. [14] for a discussion of transport coefficients in the plasma regime, where compressibility is also important.

We first introduce the dimensionless mass diffusion $\tilde{\nu}$, surface tension $\tilde{\sigma}$, viscosity $\tilde{\mu}$, and thermal conductivity $\tilde{\kappa}$ constants

$$\tilde{\nu} = \nu/(\lambda\sqrt{Ag\lambda}), \quad \tilde{\sigma} = \sigma/(\lambda^2\Delta\rho g),$$

$$\tilde{\mu} = \mu/(\lambda\sqrt{Ag\lambda}), \quad \tilde{\kappa} = \kappa/(c_p\rho\lambda\sqrt{Ag\lambda}). \tag{3}$$

Here ν, σ, μ, and κ are the corresponding dimensional parameters, c_p is the specific heat, and λ is a wavelength characterizing the initial perturbations. The wavelength of the initial disturbance is the least well determined of the quantities which enter into the dimensionless scale breaking coefficient. The theory of the most rapidly growing wavelength asserts that the observed, or true initial disturbance, in the absence of externally imposed disturbances, will have this most rapidly growing length. The growth rates are determined by dispersion relations, assuming a small amplitude initial disturbance. When considering miscible fluids, we denote the thickness of the diffusion layer as $\delta_D = 2\sqrt{\nu t}$. The dispersion relation for incompressible flow including both viscosity and mass diffusion gives the growth rate [14]

$$n = (Agk/\psi + \mu^2k^4)^{1/2} - (\mu + \nu)k^2, \tag{4}$$

where ψ is the eigenvalue of the equation

$$\frac{d}{dz}\left(\rho\frac{dw}{dz}\right) = wk^2\left(\rho - \frac{\psi}{Ak}\frac{d\rho}{dz}\right), \quad w \to 0 \text{ as } z \to \pm\infty,$$

and

$$\rho = \frac{1}{2}(\rho_1 + \rho_2)[1 + A\ \mathrm{erf}(z/\delta_D)]$$

is the density profile. The most unstable wavelength can be calculated numerically. When viscosity alone is dominant, the value of λ is determined analytically [14],

$$\lambda = \frac{4\pi\mu^{2/3}}{(Ag)^{1/3}}. \tag{5}$$

The dimensionless viscosity parameter $\tilde{\mu}$ with this theoretical wavelength is a constant, $\tilde{\mu} = 1/(4\pi)^{3/2}$. The thermal diffusivity ν_0 can be defined by

$$\nu_0 = \frac{\kappa}{\rho c_p}.$$

For incompressible fluids, the thermal diffusivity can be considered as an identical mass diffusion with mass diffusion coefficient ν_0. For immiscible fluids, one has [6]

$$\lambda = 2\pi\left(\frac{3\sigma}{g\Delta\rho}\right)^{1/2}, \quad \tilde{\sigma} = \sigma/(\lambda^2\Delta\rho g) = \frac{1}{3(2\pi)^2} = 8.5 \times 10^{-3} \tag{6}$$

for all values of g, λ, and $\Delta\rho$.

To clarify the multitude of parameters and their dependences, we have generated a data base of known RT experiments and parameters, an excerpt of which is presented in Table I. We find many cases where the theory of the most unstable wavelength agrees with observation. For related experiments of the same class, but lacking the observational data, it seems safe to infer that this theory remains valid. We note that this not only increases the number of experiments which can be modeled by our simulations, but it also removes the slightly subjective aspect of visual determination of the most unstable wavelength.

TABLE II. Mixing rates compared: FRONTIER simulation compared to experiment and ideal fluid FRONTIER compared to ideal untracked TVD. The final column (computed for simulations only) is the percentage change from the FRONTIER simulation of the ideal case.

Experiment simulation	Comment	Coeff.	α	Percentage change
Banerjee-Andrews	Mass diffusion [9]	$\tilde{\nu}=0.3$	0.07	
FRONTIER	Miscible	$\tilde{\nu}=0.3$	0.069	−23%
TVD	Untracked [13], Ideal	0.0	0.035	−61%
FRONTIER	Ideal	0.0	0.09	0%
TVD	Untracked, ideal (renormalized)	0.0	0.076	−16%
FRONTIER	Miscible, ideal (renormalized)	0.0	0.089	−1%
FRONTIER	High compressibility (renormalized)			
	Ideal, $M^2=0.25$	0.0	0.11	+22%
	Ideal, $M^2=0.5$ [13]	0.0	0.21	+133%

We also find cases where the observed wavelength and the most unstable wavelength do not even nearly coincide, and then we conclude that the observed value has been imposed by the experimental apparatus. The question of initial conditions for the experimental studies has been widely discussed [15], in the context of arguing that unobserved long wave initial perturbations affect experimentally observed mixing rates α. In contrast, we are making use of observed wavelengths somewhat longer or shorter than the most unstable wavelength.

For the case modeled here of the splitter plate air-helium experiments of Ref. [9], we have as a private communication from the author an initial disturbance wavelength of 0.5 cm. For those experiments with a series of published visual images, we can estimate an initial wavelength as the smallest observable length in the series of images.

A number of experiments have used immiscible fluids with surfactants. There are two issues which require further study in this case: the variable surfactant concentration along the interface between the fluids, and the Marangoni force resulting from variations in surfactant concentration. Until these effects have been modeled numerically, we do not attempt to simulate such experiments.

Plasma accelerated instabilities typically have machined initial perturbations with one or several wavelengths. Visually, it is clear that the dominant effect derives from the imposed wavelengths and not from the most unstable ones. Thus the simulation of instabilities with initial wavelengths other than the most unstable ones is of direct experimental interest, and the effect of scale breaking on these experiments has been identified as an important question [14].

III. SIMULATION RESULTS FOR MISCIBLE FLUIDS

We model miscible fluids using physical values for the interfluid mass diffusion. Experiments [9] studied the mixing of air and helium, with a Fickian diffusion constant $\nu=0.00066\ \mathrm{cm}^2/\mathrm{ms}$ [16]. We introduce the dimensionless diffusion constant $\tilde{\nu}=\nu/(\lambda\sqrt{Ag\lambda})=0.3$ and dimensionless time scale $\tilde{t}=\sqrt{g\lambda}$, with g=Earth's gravity, $A=0.035$ the Atwood number, and $\lambda=0.5$ the initial bubble diameter. We model this experiment with an initial $\tilde{\nu}=0.3$ and we use the Atwood number $A=0.5$.

Our simulations are based on the improved front tracking algorithm [17], which greatly minimizes the interpolative smoothing (numerical surface tension) of the interface. The grid based algorithm previously used handled bifurcations robustly, but with excess interpolation, and now the grid based reconstruction is applied only in local regions where needed and not globally as before. We use a fully Lagrangian method to propagate the interface to obtain an accurate solution of the interface position. Eulerian reconstruction of the interface is only used in small regions where topological bifurcation is detected.

The advantage of the front tracking method is to eliminate numerical mass diffusion across the interface completely. Physical mass diffusion must then be added to the calculation. In our simulations, we compute the diffused mass, based on the analytical solution of the diffusion equation in one dimension, i.e., with spectral accuracy, as the amount of mass diffused through the interface at each time step. The diffusion algorithm, based on these ideas, has been studied in detail in a separate publication [18]. It can be regarded as a type of subgrid algorithm, as its purpose is to give relatively correct simulation values when the mesh is too large to accomplish this goal through normal finite differencing. As with subgrid algorithms in general, its effect is removed as the mesh is refined. Thus the asymptotic convergence is unchanged.

Our main results, summarized in Table II, are the values for the mixing rate α for the bubble penetration into the heavy fluid, in agreement with experimental data. One simulation presented here is highly compressible ($M^2=0.25$). All the others are nearly incompressible ($M^2=0.0076$). Here $M^2=\lambda g/c_h^2$ is a dimensionless measure of compressibility, where c_h denotes the sound speed of the heavy fluid. On the

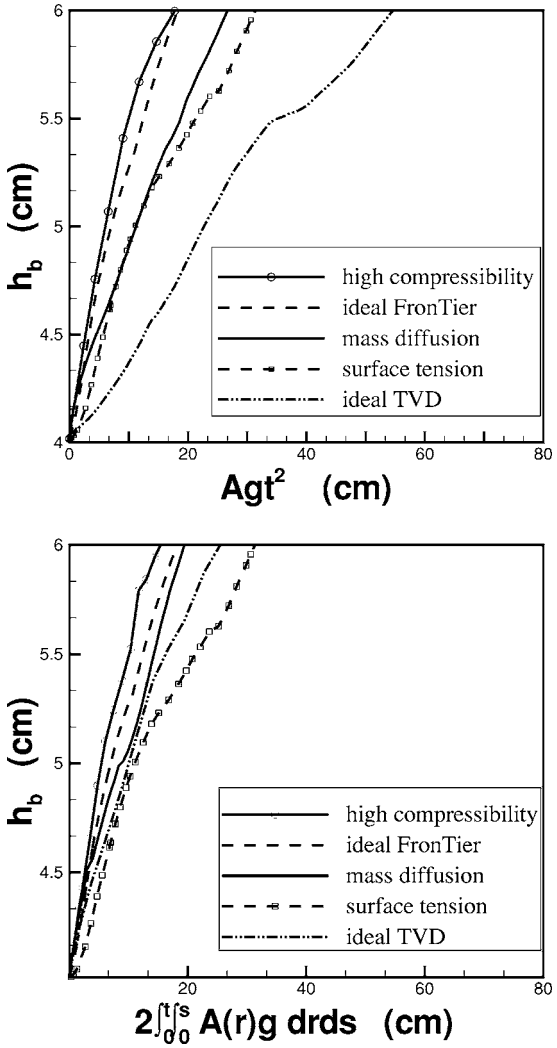

FIG. 1. Top: Self-similar growth of the mixing zone. Bottom: The same data plotted using a time dependent Atwood number, to remove the effects of numerical or physical mass diffusion and of compressible ($M^2=0.25$) density stratification. See also Table II where results from several different compressibilities are given.

basis of the results of Table II, we identify scale dependent phenomena, i.e., transport, surface tension, and compressibility, as significant contributors to the mixing rate.

We remove the effects of compressible density stratification and of various levels of numerical and/or physical mass diffusion. In this manner, we explain the various bubble penetration curves in terms of a universal theory, through the use of time dependent Atwood numbers [13]. The raw or unadjusted mixing rate is the slope of the curve h vs Agt^2. Following Ref. [13], we introduce a time dependent Atwood number $A(t)$ defined by the solution itself. Using this, we can define the variable density corrected mixing rate as the slope of h vs $2\int_0^t\int_0^s A(r)g\,dr\,ds$.

The raw and density renormalized mixing rates are plotted in Fig. 1 (top and bottom). Observe that the rescaled plots on the bottom, for two tracked simulations (ideal and physical mass diffusion), are in close agreement, indicating that the differences in the time dependent Atwood number account for the different penetration rates of these cases. The discrepancy between scaled tracked and untracked renormalized plots appears to be due to grid related interface smoothing, an effect we call numerical surface tension. The discrepancy between scaled tracked high and low compressibility is due to compressibility effects.

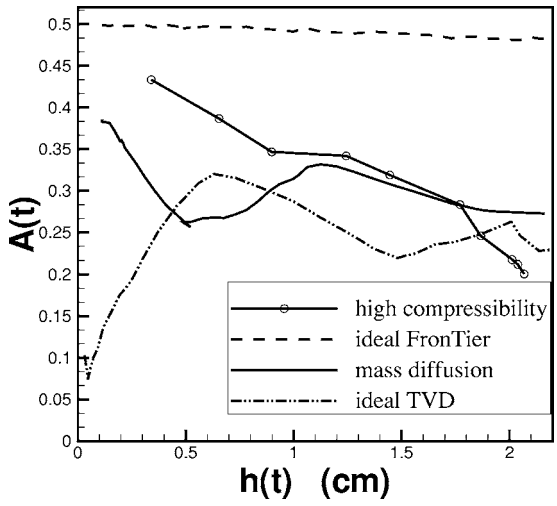

FIG. 2. Plot of the time dependent Atwood number for tracked simulations with and without physical mass diffusion and for an untracked simulation (with numerical mass diffusion).

The h vs Agt^2 and especially the renormalized h vs $\int_0^t\int_0^s A(r)g\,dr\,ds$ plots in Fig. 1 have straight line shapes after an initial transient, and we here report the slope obtained by joining the initial to the final point. We separate variable density effects from the numerical and physical surface smoothing and surface tension effects and obtain the results of Table II.

In Fig. 2, we plot the time dependent Atwood numbers [13] for the curves of Fig. 1. The deviation of the low compressibility $A(t)$ from $A=A(t=0)$ is due mainly to numerical or physical mass diffusion.

IV. THE BUBBLE MERGER PROCESS

The acceleration of the bubble envelope in multimode Rayleigh-Taylor (RT) instability is postulated to depend on the process of bubble competition and merger [11,19–23]. Key phenomena characterize this process.

(1) The proximity of bubbles to each other. Bubble competition and the merger which drives the acceleration of the bubble envelope can only occur if bubbles are sufficiently close to each other.

(2) The speed of taller vs shorter bubbles. Taller bubbles should on the average advance faster than neighboring shorter bubbles. These faster moving bubbles then expand to take up the space left by the slower, lower bubbles which, in terms of relative velocities, get swept downstream of the main bubble envelope flow. Thus there is an inverse cascade with fewer and larger structures dominating the flow as time progresses. This process is called bubble competition and merger.

(3) Speed of taller bubbles vs single mode theory. The vertical velocity of the taller multimode RT bubbles should

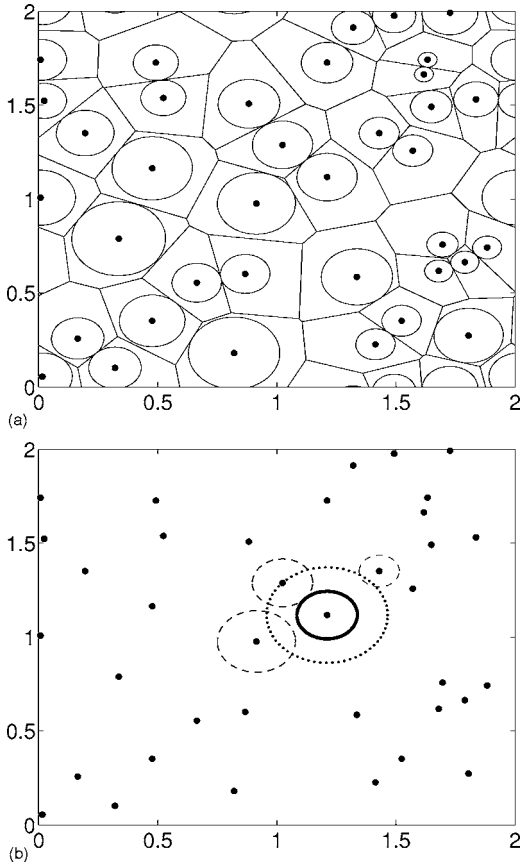

FIG. 3. Horizontal plane view of bubble tip locations at time $\tilde{t}=13.75$. (a) Voronoi diagram of the bubble tip locations in the horizontal plane, and the accompanying maximum radius circles enclosed in a Voronoi cell and centered at a bubble tip. These circles represent the bubbles. (b) Definition of the one-radius neighborhood of a bubble; the inner circle (solid line) is the bubble as defined in (a) while the outer circle (dotted line) defines a one-radius neighborhood around that bubble. The three dashed line circles represent bubbles within the one-radius neighborhood of the solid line bubble, and thus presumed to interact with it.

be considerably greater than the terminal velocity of a single bubble of an equivalent radius in single mode RT instability. The increment in velocity, called the bubble envelope velocity [24], is about equal to single mode bubble velocity [24].

We demonstrate quantitatively (with the low compressibility simulation of Sec. III) that tracked mass diffusive simulations exhibit these three characteristics. Our diagnostics therefore support the view that bubble competition and merger occurs in RT simulations, driving the acceleration of the bubble envelope.

A. Multimode vs single mode

Since Eq. (2) is used to describe the bubble penetration in multimode RT instability, it is important that the simulations remain in the multimode regime up to the latest times that Eq. (2) is used to model the bubble envelope growth. The dynamics of a single mode RT instability are very different from the multimode case. Single mode RT instability is characterized by a brief initial period of exponential growth followed by linear acceleration and then transition to an approximately constant terminal velocity v_∞ of the bubble [11,22,25,26]; multimode RT is characterized by nonlinear coupling of modes which drives continual acceleration of the bubble envelope.

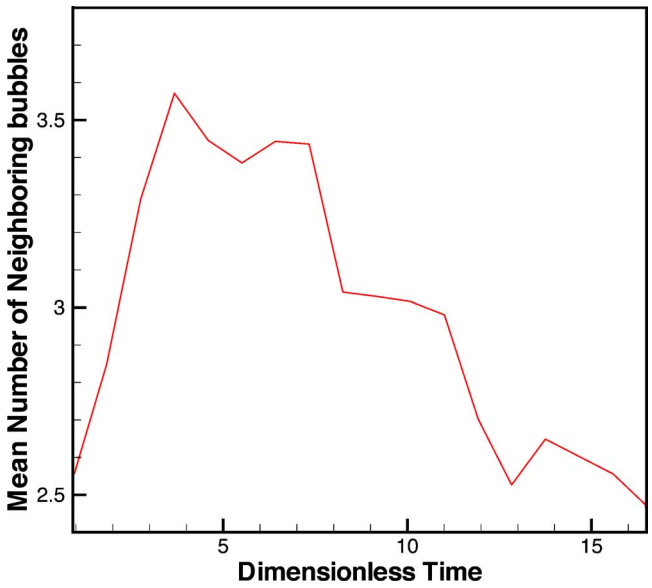

FIG. 4. (Color online) Mean number of bubbles within a one-radius neighborhood of a given bubble.

To analyze the bubble dynamics, we first identify the x,y (horizontal) plane location of the bubble peaks, and then determine the average of the number of bubbles near each bubble. We use an algorithm described in Ref. [12] to determine distinct bubble peaks above the 20% light fluid volume fraction height. To ensure the accuracy of these bubble peak locations, we compare the results of the algorithm with horizontal slices through the bubble portion of the mixing zone at and above the 20% light fluid volume fraction height. This combined approach gives accurate bubble tip locations up to dimensionless time 16.5 (the simulation runs up to dimensionless time 19.25), but the extremely complicated nature of the late time interface makes the task of identifying individual bubbles highly subjective, and none of the analysis described in this section is performed on simulation times later than $t=18$.

The radius of influence (or radius) of a bubble is defined by first considering a Voronoi cell decomposition of the horizontal plane containing the x-y location of the bubble peaks. The radius of the largest circle centered at a bubble location and enclosed in its Voronoi cell defines the radius of that bubble. Figure 3(a) illustrates this construction for $\tilde{t}=13.75$. See also Ref. [12].

We use a one bubble radius separation to determine the number of bubbles near a given bubble. See Fig. 3(b). In Fig. 4, we plot the average number of other bubbles within a one-radius neighborhood of each bubble. The average is about 3, showing that the multimodal regime is still present at late time. Bubbles are still sufficiently close to each other at late time to affect the growth pattern of other bubbles significantly; bubble competition and merger is still viable. This analysis quantitatively confirms the qualitative impres-

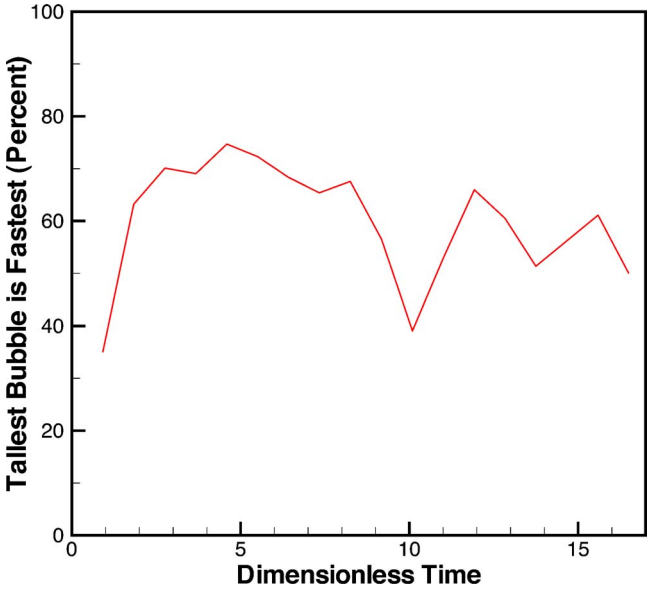

FIG. 5. (Color online) Percentage measure of the number of times the tallest bubble in a neighborhood is also the fastest advancing bubble in that neighborhood.

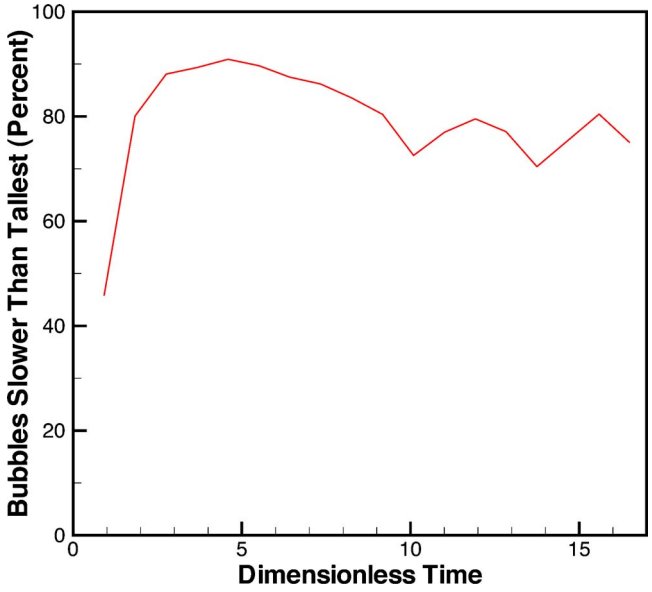

FIG. 6. (Color online) The percentage of bubbles in a neighborhood which are slower than the tallest bubble in that neighborhood.

sion obtained from late time front plots of tracked RT multimode simulations. (See, for example, Ref. [27] or [28].)

B. Vertical velocities of neighboring bubbles and inverse cascade

Using the one-radius neighborhoods defined in Sec. IV A for each bubble, we study the relationship between the vertical velocities of neighboring bubbles. The bubble competition and merger concept requires that, in general, taller bubbles advance faster than their shorter neighbors. We illustrate that this in fact happens in our front tracking mass-diffusion simulation using two metrics.

First, in Fig. 5, we show as a function of time the percentage of occurrences of the tallest bubble in a neighborhood also having the largest vertical speed. This percentage (about 60% on a time-averaged basis) can be compared with the value 25% which would result if there were no correlation between bubble height and velocity.

However, even if the tallest bubble in a neighborhood is not the fastest advancing bubble, it is typically *almost* the fastest bubble. A second metric also illustrates that taller bubbles move faster than shorter ones. For each one-radius neighborhood we determine the percentage of bubbles which are slower than the tallest bubble in that neighborhood. The weighted mean of those percentages (with the proportion of the total number of neighborhood bubbles in each neighborhood serving as the weights) is then computed at fixed time for all one-radius neighborhoods of bubbles. The results are summarized in Fig. 6. The tallest bubble typically moves faster than 80% of its neighbors. In the absence of a speed-height correlation, this value would be 50%. We therefore have quantitative confirmation that taller bubbles generally advance faster than do shorter ones in our simulation, as is characteristic of the process of bubble competition and merger.

Finally, we provide evidence that the disparity in bubble speeds results in an inverse cascade of increasing bubble sizes and decreasing number of large scale structures in the bubble envelope. In Fig. 7, the plots show, as a function of simulation time, a decreasing trend in the number of bubbles [frame (a)] and an increasing trend in the mean radius $\bar{r}$ of the bubbles [frame (b)]. Reference [23] defines an $\alpha_r = \bar{r}/Agt^2$ for which there is no known published miscible experimental value but for which the immiscible experimental value is approximately 0.01. The immiscible simulation [12] reports $\alpha_r = 0.01$ also. That value is twice as large as $\alpha_r = 0.005$ obtained from the miscible front tracking simulation, indicating a possible difference in the bubble dynamics between miscible and immiscible RT mixing.

C. Multimode velocities vs single mode terminal velocities

We compare the vertical speeds of the taller multimode RT simulation bubbles to the terminal speeds of single mode bubbles of equivalent radii. By $\tilde{t} = 1.83$, the simulation bubbles have achieved a height much greater than half their mean radius. From the rough guideline established in Ref. [25], this means that as single mode perturbations they should be entering the terminal velocity regime. However, on average, the speed of the tallest 25% of the multimode simulation bubbles is 2.4 times the corresponding single mode terminal velocity. This is consistent with the two-dimensional simulation study [24], which found increases in multimode bubble velocities by a factor of 2 over equivalent single mode bubble terminal velocities. This is further evidence that the bubble dynamics are dominated by the interaction of neighboring bubbles. These results are summarized in Fig. 8. The formula used for computing v_∞ [29] is

$$v_\infty = c_b\sqrt{Agr} = 0.48(\sqrt{Agr}), \tag{7}$$

where r is the bubble radius.

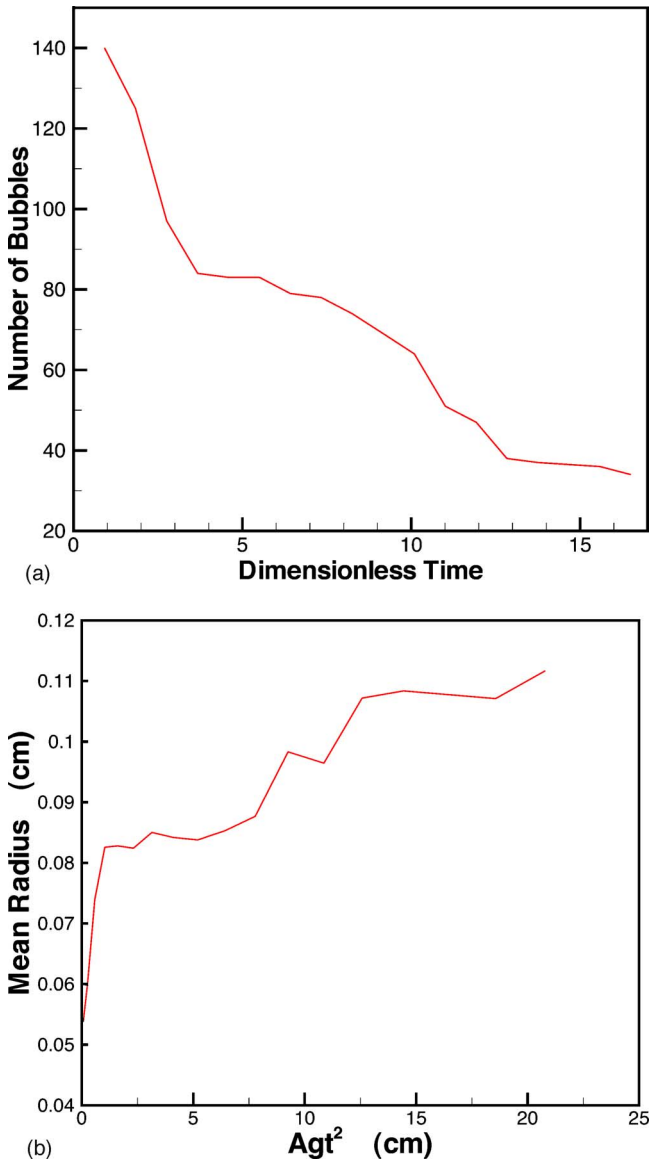

FIG. 7. (Color online) (a) The number of bubble peaks above the 20% volume fraction contour as a function of time. (b) The mean bubble radius $\bar{r}$ as a function of scaled distance.

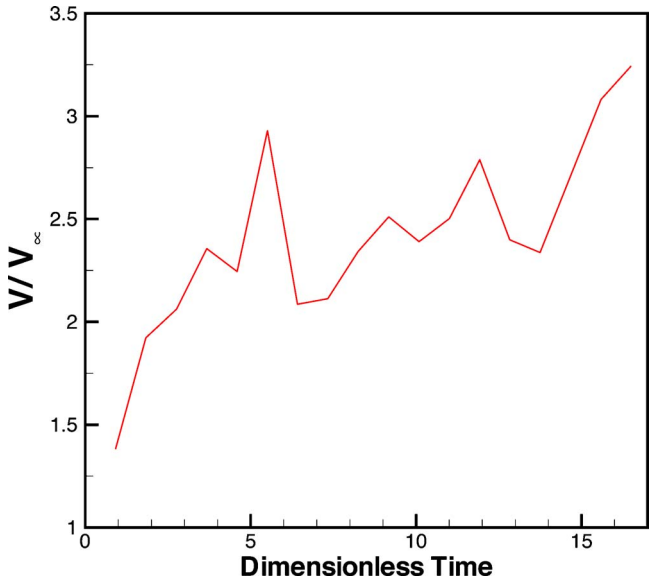

FIG. 8. (Color online) A comparison of the front tracking simulation vertical speed v of the tallest 25% of bubbles with the Taylor-formula terminal vertical speed v_∞ of those same bubbles when regarded as single isolated bubbles.

V. CONCLUSIONS

In this paper, we report a set of 3D Rayleigh-Taylor multimode mixing simulations, based on improved physics modeling and on an improved tracking algorithm in the front tracking code FRONTIER. The simulations model the experimental data of Banerjee and Andrews [9]. We include a discussion of other scale breaking physical effects: mass diffusion, surface tension, compressibility, and numerical scale breaking effects (numerical mass diffusion and effective numerical surface tension) in the analysis. The scale breaking terms cause a change in the mixing rate α ranging from over +100 to −61 % in comparison to an ideal simulation, lacking scale breaking effects. They agree with experimental values for both miscible and immiscible fluids.

Our main conclusion is that simulations in agreement with experiment for Rayleigh-Taylor mixing have been obtained. Accurate numerical tracking to control numerical mass diffusion and numerical surface tension and accurate modeling of physical scale breaking phenomena were essential to accomplish these simulations.

Remaining issues concern the data of Dimonte and Schneider [10], for which the role of surfactants requires additional physical modeling and some miscible experiments for which viscosity, not mass diffusion, is the dominant scale breaking physics. Additionally, the influence of mesh refinement should be explored when computer resources permit, but we observe that the mesh resolution per bubble used in the present study is already 2 times finer than that of the benchmark study [15].

ACKNOWLEDGMENTS

Supported in part by the U.S. Department of Energy Grant DE-AC02-98CH10886 and DEFC02-01ER25461, the Army Research office Grant W911NF0510413 and the NSF Grant No. DMS-0102480.

[1] I.-L. Chern, J. Glimm, O. McBryan, B. Plohr, and S. Yaniv, J. Comput. Phys. **62**, 83 (1986).
[2] J. Glimm, E. Isaacson, D. Marchesin, and O. McBryan, Adv. Appl. Math. **2**, 91 (1981).
[3] J. Glimm, J. W. Grove, X.-L. Li, K.-M. Shyue, Q. Zhang, and Y. Zeng, SIAM J. Sci. Comput. (USA) **19**, 703 (1998).
[4] J. W. Grove, J. Appl. Math. **14**, 213 (1994).
[5] J. Glimm, J. W. Grove, X. L. Li, W. Oh, and D. H. Sharp, J. Comput. Phys. **169**, 652 (2001).
[6] V. S. Smeeton and D. L. Youngs (unpublished).
[7] D. M. Snider and M. J. Andrews, Phys. Fluids **6**, 3324 (1994).
[8] K. I. Read, Physica D **12**, 45 (1984).
[9] A. Banerjee and M. J. Andrews Phys. Fluids (to be published).
[10] G. Dimonte and M. Schneider, Phys. Rev. E **54**, 3740 (1996).
[11] D. H. Sharp, Physica D **12**, 3 (1984).
[12] E. George, J. Glimm, X. L. Li, Y. H. Li, and X. F. Liu, Phys. Rev. E (to be published).
[13] E. George and J. Glimm, Phys. Fluids **17**, 054101 (2005).
[14] H. F. Robey, Phys. Plasmas **11**, 4123 (2004).
[15] G. Dimonte, D. L. Youngs, A. Dimits, S. Weber, M. Marinak, S. Wunsch, C. Garsi, A. Robinson, M. Andrews, P. Ramaprabhu, A. C. Calder, B. Fryxell, J. Bielle, L. Dursi, P. MacNiece, K. Olson, P. Ricker, R. Rosner, F. Timmes, H. Tubo, Y.-N. Young, and M. Zingale, Phys. Plasmas **16**, 1668 (2004).
[16] J. A. Dean, *Lange's Handbook of Chemistry* (McGraw-Hill, New York, 1999).
[17] Jian Du, Brian Fix, James Glimm, Xicheng Jia, Xiaolin Li, Yunhua Li, and Lingling Wu, J. Comput. Phys. **213**, 613 (2006).
[18] X. F. Liu, Y. H. Li, J. Glimm, and X. L. Li, J. Comput. Phys. (to be published).
[19] J. Zufiria, Phys. Fluids **31**, 440 (1988).
[20] J. Hecht, U. Alon, and D. Shvarts, Phys. Fluids **6**, 4019 (1994).
[21] U. Alon, J. Hecht, D. Ofer, and D. Shvarts, Phys. Rev. Lett. **74**, 534 (1995).
[22] X.-L. Li, B. X. Jin, and J. Glimm, J. Comput. Phys. **126**, 343 (1996).
[23] B. Cheng, J. Glimm, and D. H. Sharp, Chaos **12**, 267 (2002).
[24] J. Glimm, X.-L. Li, R. Menikoff, D. H. Sharp, and Q. Zhang, Phys. Fluids A **2**, 2046 (1990).
[25] D. L. Youngs, Physica D **12**, 32 (1984).
[26] J. Glimm, X.-L. Li, and A.-D. Lin, Acta Math. Appl. Sin. **18**, 1 (2002).
[27] E. George, J. Glimm, X. L. Li, A. Marchese, and Z. L. Xu, Proc. Natl. Acad. Sci. U.S.A. **99**, 2587 (2002).
[28] E. George, J. Glimm, J. W. Grove, X. L. Li, Y. J. Liu, Z. L. Xu, and N. Zhao, in *Hyperbolic Problems: Theory, Numerics, Applications*, edited by T. Hou and E. Tadmor (Springer Verlag, Berlin, 2003) pp. 175–184.
[29] G. I. Taylor, Proc. R. Soc. London, Ser. A **201**, 192 (1950).